



## Original article

## A novel U-net model for brain tumor segmentation from MRI images



Marwa Obayya<sup>a</sup>, Asma Alshuhail<sup>b</sup>, Khalid Mahmood<sup>c</sup>, Meshari H. Alanazi<sup>d,\*</sup>, Mohammed Alqahtani<sup>e</sup>, Nojood O. Aljehane<sup>f</sup>, Hamad Almansour<sup>g</sup>, Mohammed Abdullah Al-Hagery<sup>h</sup>

<sup>a</sup> Department of Biomedical Engineering, College of Engineering, Princess Nourah bint Abdulrahman University, PO Box 84428, Riyadh 11671, Saudi Arabia

<sup>b</sup> Department of Information Systems, College of Computer Sciences & Information Technology, King Faisal university, Saudi Arabia

<sup>c</sup> Department of Information Systems, Applied College at Mahayil, King Khalid University, Saudi Arabia

<sup>d</sup> Department of Computer Science, College of Sciences, Northern Border University, Arar, Saudi Arabia

<sup>e</sup> Department of Information System and Cyber Security, College of Computing and Information Technology, University of Bisha, Bisha 61922, Saudi Arabia

<sup>f</sup> Department of Computer Science, Faculty of Computers and Information Technology, University of Tabuk, Tabuk, Saudi Arabia

<sup>g</sup> Applied Collage, Najran University, Najran, Saudi Arabia

<sup>h</sup> Department of Computer Science, College of Computer, Qassim University, Saudi Arabia

## ARTICLE INFO

## ABSTRACT

## Keywords:

Brain tumor segmentation  
Deep learning  
U-Net architecture  
Dice Loss/IoU  
LGG Segmentation Dataset

Segmentation of brain tumors aids in diagnosing the disease early, planning treatment, and monitoring its progression in medical image analysis. Automation is necessary to eliminate the time and variability associated with traditional segmentation methods. Convolutional neural networks (CNNs) and U-Net architectures have demonstrated their efficiency and effectiveness in segmenting brain tumors from MRI images using deep learning techniques. The paper presents an improved U-Net-based segmentation algorithm that integrates nested skip paths to improve encoder-decoder feature fusion. The performance of segmentation was optimized by utilizing a variety of activation functions and loss functions, including Dice Loss and Intersection over Union (IoU). A high level of accuracy was demonstrated in the proposed model when it was evaluated using the LGG Segmentation Dataset. The proposed approach for segmenting medical images has been shown to be both robust and efficient in a comparative analysis.

## 1. Introduction

A critical function of medical image analysis is segmenting brain tumors so that they can be accurately identified and classified from MRI images. It is essential to accurately segment brain tumors in order to diagnose the disease, plan treatments, and monitor the progression of the disease. Due to time and error-prone manual segmentation, expert intervention is necessary. Medical images can be segmented using various deep learning algorithms, including convolutional neural networks (CNNs). An abnormal growth or tissue within the human body is a tumor. Tumors are composed of groups of cells. A tumor can be malignant, which means it is cancerous, or benign, which means it isn't cancerous [1,2]. A physician may have difficulty manually identifying these abnormal growths due to their time-consuming and onerous nature. This necessitates the development of intelligent systems that can automatically detect cancerous cells in a particular area of the body [3, 4]. As technology advances in the medical field, diagnostics and

predictive analysis have become increasingly sophisticated. A number of healthcare analysis services have advanced, including the segmentation of brain tumors [5], the prediction of heart disease [6,7], stroke prediction, identifying stroke indicators, and the detection of ECG abnormalities in real-time.

Evaluating the model's segmentation performance on noisy MRI scans is important to assess its robustness under real-world conditions. Future work will investigate how the model performs on MRI scans with different types of noise, such as Gaussian noise or motion artifacts, which commonly occur in clinical settings. Techniques such as data augmentation, noise reduction methods, and adversarial training will also be explored to improve the model's resilience to noisy inputs [8].

In the human skull, tumors occur as abnormal growths. To examine the brain, it is necessary to use noninvasive technology, such as electroencephalography. The use of magnetic resonance imaging (MRI) for the diagnosis of brain tumors is one method of diagnosis. A patient's brain is scanned in three dimensions, and the images can be viewed in

\* Corresponding author.

E-mail address: [Meshari.alanazi@nbu.edu.sa](mailto:Meshari.alanazi@nbu.edu.sa) (M.H. Alanazi).

one of the three planes (Coronal, Sagittal, and Transversal). An abnormal growth within the cranium can be identified by each perspective plane. A perspective plane-based MRI classification method has improved cancer detection accuracy with MRIs [9]. In the case of a brain tumor, MRI can be used to assess its size and location using brain tumor segmentation. Rather than relying on manual features, deep learning networks can segment images according to regions of interest (ROIs). Some areas have demonstrated success with deep learning [10, 11], but in order for them to be successful, they require either large quantities of annotated data or aggressive data augmentation [12].

A variety of applications are found in the worlds of image processing and computer vision that rely on image segmentation [13,14]. Assigning each pixel to a different object in the image is the challenge. The task of solving this problem has been addressed by a number of algorithms over the years [15]. Medical imaging has also made extensive use of the process of segmentation. In previous studies on MRI scans, a lot of image segmentation techniques have been modified in order to manipulate the volumetric images in three dimensions [16,17]. In addition to modifying the networks, the performance of the given task is further improved. Studies have shown that MRI characteristics can serve as indicators of a probable diagnosis and treatment strategy for new brain tumors [18,19]. In addition to assessing tumor cellularity, vascularity, and blood-brain barrier integrity using MRI, multimodal MRI can also provide information about tumor vascularity and blood flow. It is important to note, however, that multimodal MRI protocols produce a wide variety of image contrasts that provide complementary information. MRI protocols for brain tumors typically involve T-1- and T-2-weighted MRIs as well as gadolinium-enhanced T-1-weighted MRIs. In most cases, structural MRI images are helpful in diagnosing conditions [20]. A critical part of studying brain tumors with MRI images is segmenting the image: (1) segmentation of the brain tumor allows the elimination of confounding structures from other brain tissues, resulting in more accurate classifications of brain tumors and more accurate diagnoses. (2) It is critical to accurately delineate the extent of the brain tumor when planning radiotherapy or surgery, ensuring that healthy tissues surrounding it are excluded to prevent damage to the areas of language, motor, and sensory functions during treatment[21]. By segmenting longitudinal MRI scans, brain tumors can be tracked for growth, recurrence, and shrinkage.

Exploring additional MRI modalities beyond FLAIR could enhance segmentation accuracy by leveraging complementary information from different imaging sequences. Future work will investigate the impact of incorporating T1, T2, and DWI modalities, either individually or through multimodal fusion, to improve feature representation and tumor differentiation. The contribution of different modalities to model performance will also be assessed, along with an exploration of optimal fusion strategies for enhanced segmentation. A brain tumor occurs when abnormal brain cells grow in the brain, and they are among the most common abnormalities of the brain. Multiple brain regions are responsible for different functions of the nervous system, which makes the brain's structure complex [22]. In addition to the protective linings of the brain and skull, tumors may also develop in the base of the brain. A brain tumor can be classified according to the tissue from which it originated [23]. In particular, U-NET, a convolutional network architecture used for segmenting biomedical images, is proving highly effective. MRI images can be segmented into regions of interest based on features captured by the encoder-decoder structure, which is well suited to segmenting brain tumors.

Class imbalance is a critical challenge in medical image segmentation, particularly for accurately detecting smaller tumor regions. Future work will incorporate strategies such as weighted loss functions to give more importance to underrepresented classes. Additionally, data augmentation techniques, such as synthetic data generation and oversampling, will be explored to improve model robustness against class imbalance. Differentiating between tumor subregions, such as necrotic and enhancing areas, is crucial for a more detailed and clinically

relevant segmentation. Future work will explore multi-class segmentation techniques to classify and distinguish these tumor subregions more effectively. This will include training the model with annotated datasets that specifically label different tumor regions and incorporating advanced loss functions, such as weighted Dice loss, to improve performance.

Investigating the impact of deeper encoder-decoder architectures, particularly in relation to segmentation performance, is crucial. While the current model demonstrates improved feature fusion, exploring deeper architectures could potentially provide further performance gains by capturing more complex patterns and details in the images. The performance of different architectures will also be compared to identify the optimal depth for improving brain tumor segmentation from MRI images.

## 2. Related work

An MRI image of a brain tumor is used in [24] to solve a binary classification problem, using AlexNet and VGG16 to extract features and recurrent feature elimination (RFE) to eliminate redundant features. As a final step, they used an SVM for classification, which provided 96 % accuracy. As part of the tumor detection and segmentation process, the Author [25] used superpixel techniques as well as transfer learning. Through the use of superpixels, tumours were divided into two groups. According to the dice index, 0.93 was better than 0.89 on the ground truth. Brain tumor segments can be segmented by using unsupervised learning and clustering based on certain similarity criteria. A 73 % segmentation accuracy was achieved using a combination of fuzzy clustering and region-growing on CT images scanned by either T1 or T2 weighted sequences [26]. The framework was demonstrated to be feasible only with a few datasets, but it displayed promising results when segmenting multimodal MRI brain tumors [27]. Several clustering algorithms, including k-means and fuzzy k-means, as well as Gaussian mixtures, were evaluated using glioblastoma segmentation [28]. In this study, however, not even the best algorithm achieved an accuracy rate higher than 77 %.

The authors used deep neural networks in conjunction with CNN models to generate reliable MRI scan findings in [29] and [30]. A CNN architecture consisting of three layers was presented, including a backbone of fully connected neural networks. There was a 97.33 % F-score and a 96.05 % accuracy. Using the BRATS 2015 dataset, an algorithm (VGG19 pre-trained network) was developed to extract tumours and transfer learning was used to classify tumors, achieving 98.32 accuracy [31]. According to [32], segmentation tasks can be performed using OKM. There are two main concepts in the OKM method: Otsu thresholding and K-Means clustering. In all cases, the dice coefficient exceeded 0.70. By using an active contour model and semi-automated segmentation, the author [33] examined whether brain tumors had been detected on MRI T1-weighted images. It is described in [34] that RESNet50 has been modified and enhanced to differentiate between tumors and non-tumors based on MRI images. DENSENet, AlexNet, and GoogleNet are compared with the results of this study. A 97 percent accuracy rate was achieved using the proposed method in [35] by exploiting classification accuracy and error rate effects on data preprocessing. Data overfitting was reduced through augmentation methods. Models are trained and tested using the Resnet50 architecture after MRI scans are enlarged.

The importance of data augmentation in improving model robustness against variations in MRI scans is acknowledged. Future work will clarify the augmentation techniques used and evaluate their impact on model performance. Techniques such as rotation, scaling, intensity normalization, and contrast adjustments will be explored to enhance the model's ability to generalize across different MRI scan variations.

Based on 2D slices from the MRI image, the author [36] proposed a convolutional neural network segmentation method for detecting brain tumors. Additionally, two training phases were used to deal with

unbalanced input data classes. Based on a two-path architecture, the author determined the best location for multi-scale feature maps to be extracted and integrated into the Deep Medic 3D network [37]. Radiologists' expertise is required to segment images manually, which is tedious, time-consuming, and requires lots of effort. Brain scan volumetric has become increasingly segmented automatically by professionals. MRI images were automatically BTSe with a variety of solutions. Biomedical image segmentation is one of U-Net's main focuses. In only a few training samples, it achieved good segmentation results, which made it popular [38].

The potential for real-time segmentation applications in clinical workflows is an important aspect to address. Future work will discuss how the proposed method can be optimized for real-time performance, including the use of hardware acceleration (e.g., GPUs or edge computing) and techniques to reduce inference time, such as model pruning or quantization. Additionally, the integration of the model into clinical workflows will be explored to provide timely results for medical professionals, ensuring both efficiency and accuracy as mention in Table 1.

### 3. Methodology

We used U-Net to segment tumors and analyzed the effects of varying various parameters. Presented here is a method that consists of two steps: preprocessing and segmentation of data. Segmentation was implemented after preprocessing the MR scans. A segmented tumor region's performance can be quantified with this performance measure. Fig. 1 illustrates the proposed UNet model. While the nested skip connections enhance feature fusion in the proposed model, it is important to analyze their computational overhead compared to alternative architectures like Attention U-Net. Future work will conduct a comparative analysis of the computational complexity, including inference time, memory consumption, and model size, between the proposed method with nested skip connections and other architectures such as Attention U-Net. This analysis will help better understand the trade-offs between segmentation performance and computational efficiency.

#### 3.1. Proposed UNet

We propose an enhanced architecture for brain tumor segmentation that addresses semantic gaps through nested skip pathways. These pathways allow us to incorporate low-level and high-level encoder functions seamlessly, thus integrating encoders at different resolutions. Through this fusion of features, the model is better able to understand the nuances within the images.  $x^{ij}$  represents the output of node  $X$ , where  $i$  represents the down-sampling layer along with the encoder and  $j$  represents the convolution layer. To calculate  $x^{ij}$ , we use the equation below:

$$x^{ij} = \begin{cases} H(x^{i-1j}), if j = 0 \\ H([x^{ik}]_{k=0}^{j-1} u(x^{i+1j-1})) , if j > 0 \end{cases} \quad (1)$$

Following a convolution operation, there is an activation operation, and an upsampling layer is represented by  $u()$ , with  $[]$  representing their combination [47]. Our implementation of UNet establishes skip pathways between EfficientNetB7 encoders and decoders via dense skip links, as shown in Fig. 2. Through dense convolution blocks along skip pathways, previous feature maps can be aggregated at each node, enhancing segmentation accuracy and gradient flow [47].

The proposed UNet used an EfficientNetB7 encoder-decoder structure as part of its architecture design. Skip connections convolutional lower-level feature maps with upper-level feature maps prior to propagation. With dense convolution blocks, layers with related feature maps can be linked directly, reducing the semantic distance between encoder and decoder feature maps, facilitating optimizer optimization. The

**Table 1**  
Existing research comparison based on their results and findings.

Architecture	Performance metrics	Results	Key findings
3D U-Net [39]	Segmentation accuracy	Extensive experience in segmenting brain tumors from MRI datasets.	A powerful CNN model using deep learning U-Net can predict the presence or absence of a tumor.
U-Net with ResNet50 encoder [40]	Many factors determine the accuracy, precision, recall, and specificity of dice.	There are 0.008768 dice losses, 0.7542 IoUs, 0.9870 F1, 0.9935 accuracy, 0.9852 precision, 0.9888 recall, and 0.9951 specificity for this model.	Based on all performance metrics, the model performed better than the edge-based approach.
SEResU-Net [41]	Dice similarity coefficients	WT, CT, and ET had respective Dice similarity coefficients of 0.9373, 0.9108, and 0.8758.	Multimodal brain tumors are segmented more efficiently using SEResU-Net.
U-Net-VGG16 [42]	Correct classification ratio (CCR)	Data recognized by UNet-VGG16 has a CCR value of 95.69 %.	The model architecture hybrid U-Net VGG16 transfers Learning simplifies architecture.
Efficient U-Net Architecture [43]	Dice similarity coefficients	A total tumor coefficient of 0.8741, a core tumor coefficient of 0.8069, and an enhancing tumor coefficient of 0.7033 were achieved.	Based on the BraTS2020 dataset, the results show good dice similarity for the different types of tumors segmented by this method.
CU-Net [44]	Dice score	The model achieved an 82.41 % Dice score, surpassing two other current models.	As a result of its symmetrical U-shaped structure, the CU-Net model is able to segment images at high resolution by using convolutional layers, maximum pooling, and upsampling operations.
CNN with ResNet50 and U-Net [45]	IoU, DSC, SI	IoU: 0.91, DSC: 0.95, SI: 0.95.	This model outperformed all others in classifying and segmenting tumors correctly.
BU-Net [46]	Dice score	The BU-Net technique performed better than existing techniques.	U-Nets use residual extended skips (RES), wide contexts (WC), and a customized loss function as their baseline architecture.

importance of benchmarking the computational complexity of nested skip connections against alternative architectures such as Attention U-Net is acknowledged. Future work will conduct a comparative analysis to evaluate the trade-offs between segmentation performance and computational efficiency. This will include measuring inference time, memory consumption, and model complexity to determine whether Attention U-Net or other architectures provide a more optimal balance between accuracy and efficiency.

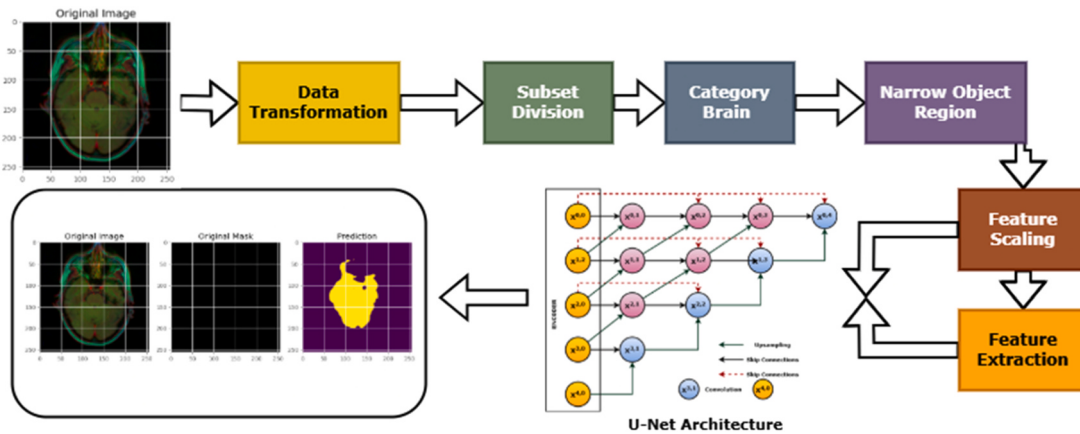


Fig. 1. The working layout of the UNet model.

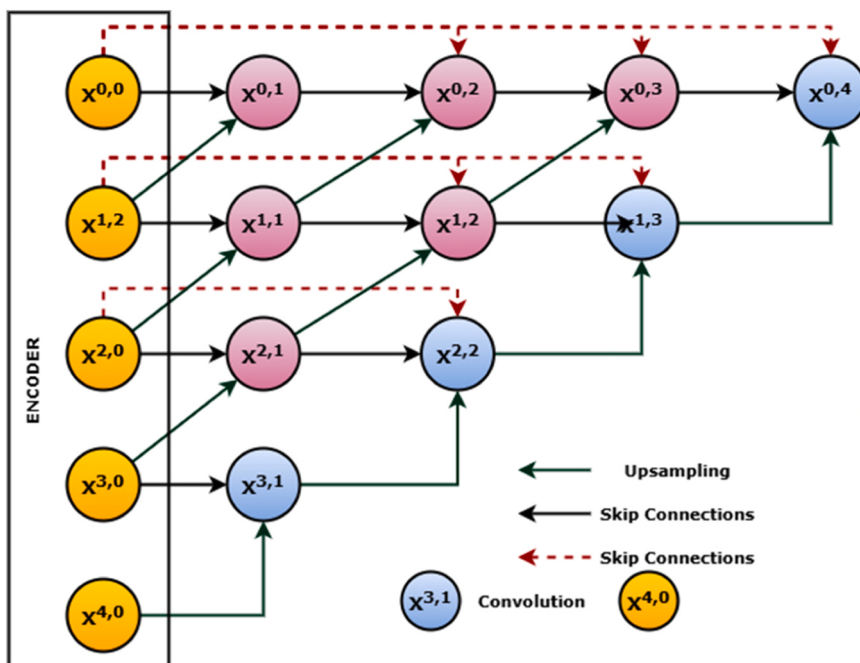


Fig. 2. Systematic representation of proposed UNet architecture.

### 3.2. Activation function

Neural networks rely heavily on activation functions. Depending on the input and biases, the weighted sum is computed, which decides whether to fire neurons. This data is manipulated through gradient descent, with certain outputs being produced by the network as a result. There are two types of activation functions or transfer functions: linear and nonlinear. Our data segmentation process is based on nonlinear activation functions, like Tanh's, ReLU's, Leaky ReLU's, ELU's, and PReLU's. Our study has demonstrated that these activation functions are superior to commonly used sigmoid functions due to their ability to reduce vanishing gradients significantly.

**Tanh function:** In deep learning, hyperbolic tangent functions, or Tanh functions [48], are used to activate neural networks. An integral function with a range of  $-1\text{--}1$  and centred at zero, there is no centre in this function, making it smooth. As shown below, we can formulate the tanh function (2).

$$f(x) = \left( \frac{e^x - e^{-x}}{e^x + e^{-x}} \right) \quad (2)$$

Tanh functions perform better than sigmoid functions in multilayer neural networks and also aid in backpropagation. Vanishing gradients, however, cannot be efficiently solved by it. Some neurons may die when Tanh reaches a gradient of 1 if no input values are provided.

- **ReLU function:** Deep learning applications use ReLU [48] - the rectified linear unit function - is an activation function widely used in deep learning applications. In addition to preserving the properties of the linear model, the ReLU can be easily optimized with gradient methods as it is analogous to a linear function. Due to the fact that this function does not use any complex operations, it provides faster computation. Whenever the input value is less than zero, this function forces it to zero, whereas when there are fewer input values, it remains unchanged. As a result, the vanishing gradient problem is nearly eliminated. Eq. (3) defines the ReLU function:

$$f(x) = \max(0, x) \quad (3)$$

It is easier to over-fit the tanh function than the sigmoid function. However, using dropout could reduce over-fitting. There may also be a dying ReLU problem, where the output always equals the input due to weights being learned with a large negative bias. The function will likely recover once it reaches this state, hence the use of Leaky ReLU or PReLU activation functions.

- **Leaky ReLU function:** According to Leaky ReLU [49], dying ReLU can be prevented by adding a small negative slope. As a result, the weights remain alive throughout the propagation process. The gradients are never zero during training but are affected by an alpha parameter. Using Eq. (4), we can define a leaky ReLU mathematically as follows:

$$f(x) = \begin{cases} x, & \text{if } x > 0 \\ ax, & \text{if } x \leq 0 \end{cases} \quad (4)$$

There are no limitations associated with a leaky ReLU, yet the results are similar to those of a standard ReLU. Leaky ReLU rather than ReLU has not been shown to produce different results in certain models.

- **Parametric ReLU function:** The Parametric PReLUs [49] are variations on ReLU activation functions. Adaptive learning is used in PReLU to learn the negative part, while linear learning is used for the positive part. Backpropagation is used here to learn the small constant ( $a$ ). In the case where the constant becomes zero, it will act as a function to activate the ReLU. It is possible to state the ReLU (Eq. (5)) as follows:

$$f(x) = \begin{cases} x, & \text{if } x > 0 \\ ax, & \text{if } x \leq 0 \end{cases} \quad (5)$$

Quantifying the influence of different activation functions on model performance through ablation studies is essential for understanding their individual contributions. Future work will conduct ablation studies by systematically testing different activation functions (e.g., ReLU, Leaky ReLU, ELU, PReLU) and evaluating their impact on key performance metrics such as segmentation accuracy, convergence speed, and robustness. This will determine which activation functions provide the best performance for the task of brain tumor segmentation.

- **ELU function:** Deep neural networks can be improved by using exponential linear units or ELUs, another variant of activation functions. For positive values, the ELU function utilizes identity, minimizing the problem of vanishing gradients. In this case, to reduce bias shifting and computational complexity, we push the mean activation close to zero with a negative value. An equation using a hyperparameter regulates the saturation point when negative values are present. This activation function has one major problem. It does not centre the values at zero. An alternative to it is the ELU function (Eq. (6)):

$$f(x) = \begin{cases} x, & \text{if } x > 0 \\ a\exp(x) - 1, & \text{if } x \leq 0 \end{cases} \quad (6)$$

### 3.3. Loss function

In this paper, two loss functions are proposed as a basis for segmenting brain tumors: Dice loss (Dice loss) and IOU. Combining these aspects allows us to create a model that effectively balances two critical components: classification accuracy and spatial overlap, both of which

are crucial when it comes to accurately identifying brain tumor regions from MRI scans. Using the loss, tumors and non-tumors can be classified accurately based on how similar their predictions are to the ground truth. When it comes to tasks that require precise delineation of tumor boundaries, especially those that involve binary classification, this is crucial. Dice loss is calculated by labelling datasets with predicted probabilities and crushed fact tags. In the Dice loss component, the spatial agreement between predicted and true binary masks is measured by taking into account how the segmented and actual tumor

The use of multiple loss functions can be beneficial for optimizing segmentation performance, but a comparative study of their individual impact is important. Future work will conduct a detailed analysis of how each loss function (e.g., Dice loss, IoU loss) contributes to segmentation accuracy and its ability to handle specific challenges like class imbalance or boundary precision. This will help better understand the strengths and weaknesses of each loss function in the context of brain tumor segmentation. Through the use of a spatial overlap metric, the proposed model can capture fine details and accurately delineate tumor boundaries regardless of how irregular or complex the tumor shape is.

$$\text{Dice loss} = 1 - \frac{2 \sum_{i=1}^N p_i g_i}{\sum_{i=1}^N p_i^2 + \sum_{i=1}^N g_i^2} \quad (7)$$

For sample  $i$ ,  $p_i$  represents predicted probability while  $g_i$  represents ground truth label. The loss functions in our model enable the MRI image to be segmented accurately based on the dataset characteristics and segmentation tasks. A common multiclass classification problem is solved using Eq. (8) which specifies a categorical cross-entropy loss function [37].

$$\text{Loss} = - \sum_{i=1}^n l_i \log(p_i) \quad (8)$$

$P_i$  is the probability for an  $i^{th}$  class to have Softmax,  $l_i$  is the truth label, and  $N$  is the number of classes. Eq. (9) contains the equation for the Jaccard Index, which is commonly used in semantic segmentation.

$$\text{Mean IOU} = \frac{TP}{FN + FP + TP} \quad (9)$$

The mean IoU can be determined by dividing the overlapped area between the predicted and ground truth segments by the area of union between them. While the  $5 \times 5$  grid visualization is useful for showing segmentation results, incorporating heatmap-based feature importance analysis could provide deeper insights into the model's decision-making process. Future work will integrate techniques such as Grad-CAM or Integrated Gradients to generate heatmaps that highlight the regions of the MRI scans most influential for the model's predictions. This will allow for a more interpretable analysis of how the model focuses on different tumor areas and help identify potential improvements.

Models consist of contracts and expansions. Convolutional networks typically reduce/contract images by downsampling them. The number of samples is reduced by applying two  $3 \times 3$  convolutions repeatedly, and then applying a rectified linear unit (ReLU) between each convolution. Every time the downsampling process is applied, the number of feature channels is doubled. Each feature map in the expansive path is first upsampled, then convolutioned twice to reduce the number of channels in half, then concatenated with the proportionately cropped feature maps in the contracting path, followed by a ReLU. When convolutions are performed, border pixels are lost, so cropping is essential. The final layer uses a  $1 \times 1$  convolution to subdivide each 64-component feature vector into relevant classes. The given network consists of 23 convolutional layers. Assessing the computational efficiency of the model during inference on low-end GPUs or CPUs is crucial for ensuring its feasibility in real-world, resource-constrained environments. Future work will evaluate the model's inference time, memory usage, and overall computational demands on various hardware configurations. Additionally, optimization techniques such as model quantization,

pruning, and batch processing will be explored to improve efficiency without compromising performance. Comparing the current deployment framework, which uses Anaconda and Spyder, with cloud-based solutions such as TensorFlow could provide valuable insights into improving scalability and deployment efficiency. Future work will involve conducting a comparative analysis of the performance, scalability, and resource usage of the model when deployed on cloud platforms like TensorFlow, especially in terms of handling large datasets and real-time inference. The benefits of using cloud resources for distributed training and inference will also be explored to further enhance the model's scalability and efficiency.

Cross-validation across multiple institutions would enhance the generalizability of the model by ensuring it performs well on diverse datasets. Future work will evaluate the model using multi-institutional datasets to assess its robustness across different scanning protocols, MRI machines, and patient demographics. Additionally, domain adaptation techniques will be explored to improve the model's ability to generalize to unseen data. The choice of batch size can significantly impact model stability and accuracy during training. Future work will explore the effects of different batch sizes on both model performance and training stability. This will include testing a range of batch sizes to assess their influence on convergence speed, generalization ability, and overall segmentation accuracy. Additionally, the interaction between batch size and other hyperparameters, such as learning rate and optimizer choice, will be investigated to optimize the training process.

#### 4. Result analysis and discussion

Often, convolutional neural networks are used to segment medical images. It was first proposed as a method of segmenting biological cell images, but it has since been extended to segmenting brain tumors in MRI images as well. Using the proposed model, convolutional and pooling layers connect encoders and decoders. Using the encoder's features, decoding reconstructs the segmentation map from the input image. U-nets also include skip connections, which improve segmentation accuracy by transferring information between the encoder and decoder. Fig. 3 shows how layer and filter numbers can be adjusted to optimize U-nets for specific tasks.

Evaluation of the proposed model was carried out using the LGG

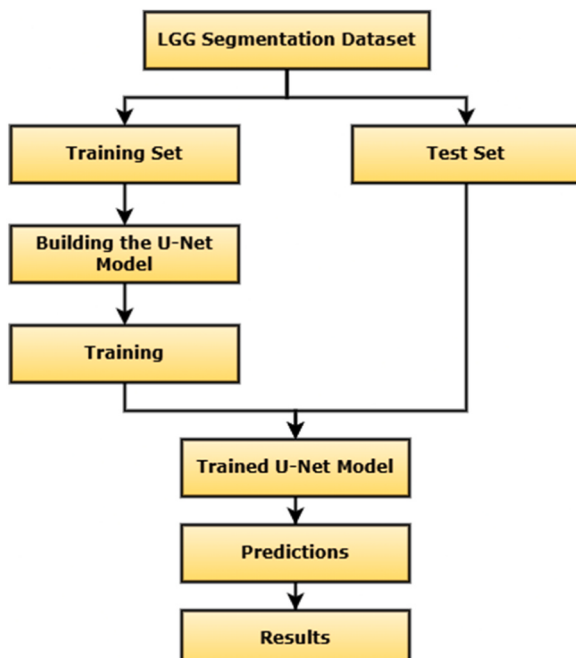


Fig. 3. Implementation procedure of the proposed model.

Segmentation Dataset. In this dataset, MR images of the brain are combined with FLAIR masks to segment abnormalities. TCIA provided the images below. A sufficient number of FLAIR sequences and clusters were available for 110 patients with lower-grade glioma in The Cancer Genome Atlas. A CSV file containing tumor genomic clusters is provided with the patient data. An image-mask pair from a dataset is visualized in Fig. 4. This command creates a five-by-five grid of subplots using matplotlib and iterates over 25 samples. The subplots display an image with an overlaid mask at 40 % transparency ( $\alpha = 0.4$ ). (Figs. 5 and 6)

Evaluating the model's robustness on larger and more diverse datasets is essential for ensuring its generalization to a broader population. Future work will involve testing the model on larger datasets, such as the BraTS dataset or other multi-institutional collections, which contain a more diverse range of MRI scans, patient demographics, and tumor types. This will help assess the model's ability to generalize across different clinical scenarios and imaging protocols. The transparency level of 40 % for overlay visualization is subjective, and a more objective, quantitative assessment of segmentation boundary accuracy is essential. Future work will include quantitative metrics such as the Hausdorff Distance, boundary mismatch, or pixel-wise accuracy to assess the precision of the segmented tumor boundaries. This will provide a clearer and more objective evaluation of how well the model delineates tumor regions.

Nvidia GPUs are used to train the model, and it takes less than 5 hours. A 50-epoch training cycle is implemented using the Anaconda and Spyder frameworks. These figures illustrate the segmentation of the best-performing model, along with its accuracy and loss. Model optimization was performed using Adam's optimizer with a learning rate of 0.001. A binary accuracy metric, intersection over union metric, and dice coefficient metric were used to model the model.

While the training time on NVIDIA GPUs is an important metric, assessing the inference time for real-world applications is equally crucial. Future work will evaluate the model's inference time on various hardware configurations, including low-end GPUs, CPUs, and edge devices, to better understand its performance in resource-constrained environments. This will help determine the model's feasibility for real-time clinical deployment and guide potential optimizations to reduce inference time without compromising accuracy. Data augmentation plays an important role in improving model robustness against variations in MRI scans. Future work will clarify the augmentation techniques used and evaluate their impact on model performance. Techniques such as rotation, scaling, intensity normalization, and contrast adjustments will be explored to enhance the model's ability to generalize across different MRI scan variations.

A fixed learning rate of 0.001 is a standard choice, but implementing an adaptive learning rate strategy could enhance convergence and overall model performance. Future work will explore techniques such as learning rate scheduling, adaptive optimizers (e.g., Adam, RMSprop), and cyclical learning rates to dynamically adjust the learning rate based on training progress. This approach may help improve stability, prevent suboptimal convergence, and accelerate training efficiency. Comparing Adam's optimizer with alternative optimization algorithms such as RMSprop or SGD could provide valuable insights into the model's performance. Future work will conduct a comparative analysis of these optimization algorithms to assess their impact on training stability, convergence speed, and overall segmentation accuracy. This will help identify the most effective optimizer for the specific task and provide a deeper understanding of how different optimization strategies influence model performance.

Brain images can be segmented optimally using our method. Despite not using all three types of MRI images in this method, a good result was obtained for the whole tumor segmentation. Based on the comparison results, we were able to achieve the best results on the Dice coefficient from the whole tumor area. As shown in Fig. 7, our experiment significantly improved the IoU of the networks and enabled faster convergence of our loss models. In our experiment, increasing the filter values

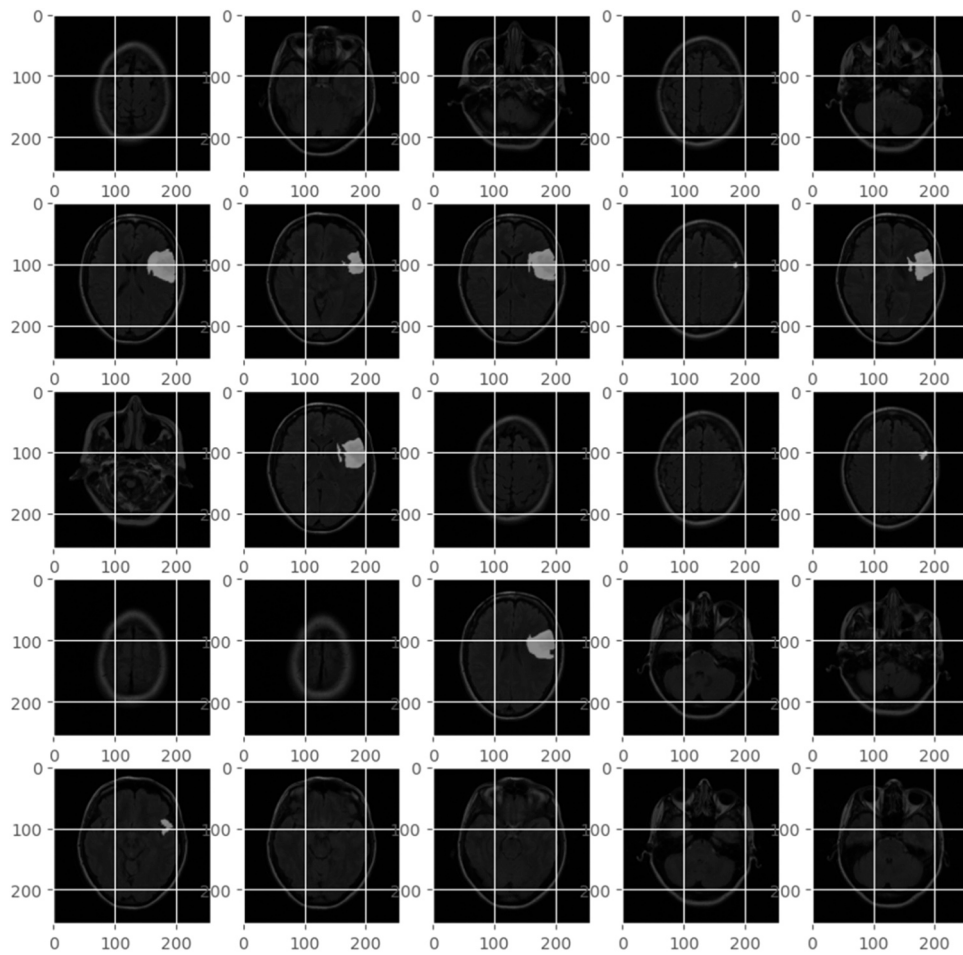


**Fig. 4.** Data visualization of image-mask pairs from a dataset.

```

Epoch 1: val_loss improved from inf to -0.02677, saving model to unet_brain_mri_seg.keras
10/10 80s 2s/step - binary_accuracy: 0.5657 - dice_coef: 0.0387 - iou: 0.0201 - loss: -0.0387 -
Epoch 2/50
10/10 0s 512ms/step - binary_accuracy: 0.8062 - dice_coef: 0.0552 - iou: 0.0290 - loss: -0.0552
Epoch 2: val_loss did not improve from -0.02677
10/10 7s 706ms/step - binary_accuracy: 0.8087 - dice_coef: 0.0561 - iou: 0.0295 - loss: -0.0561
Epoch 3/50
10/10 0s 516ms/step - binary_accuracy: 0.9029 - dice_coef: 0.0739 - iou: 0.0391 - loss: -0.0739
Epoch 3: val_loss did not improve from -0.02677
10/10 7s 712ms/step - binary_accuracy: 0.9030 - dice_coef: 0.0745 - iou: 0.0394 - loss: -0.0745
Epoch 4/50
10/10 0s 520ms/step - binary_accuracy: 0.9332 - dice_coef: 0.0565 - iou: 0.0298 - loss: -0.0565
Epoch 4: val_loss did not improve from -0.02677
10/10 10s 1s/step - binary_accuracy: 0.9338 - dice_coef: 0.0571 - iou: 0.0302 - loss: -0.0571 -
Epoch 5/50
10/10 0s 524ms/step - binary_accuracy: 0.9402 - dice_coef: 0.1181 - iou: 0.0638 - loss: -0.1181
Epoch 5: val_loss improved from -0.02677 to -0.04125, saving model to unet_brain_mri_seg.keras
10/10 12s 1s/step - binary_accuracy: 0.9404 - dice_coef: 0.1176 - iou: 0.0635 - loss: -0.1176 -
Epoch 6/50
10/10 0s 527ms/step - binary_accuracy: 0.9702 - dice_coef: 0.1664 - iou: 0.0943 - loss: -0.1664
Epoch 6: val_loss did not improve from -0.04125
10/10 7s 728ms/step - binary_accuracy: 0.9694 - dice_coef: 0.1649 - iou: 0.0934 - loss: -0.1649

```

**Fig. 5.** Result summary with respect to epoch.

three times and training the network for 50 epochs with the entire dataset directly improved segmentation performance. A comparison of the performance metrics of architectures is shown in Fig. 7. Using U-Net encoder architecture, segmentation accuracy was 0.9915, dice loss was -0.4596, IoU was 0.3132, dice\_coef was 0.4596, and dice\_coef was 0.4596. This figure shows how the loss was performed, the DICE accuracy graph score, and the IOU score according to the number of epochs.

Incorporating additional metrics, such as Hausdorff Distance, would

provide a more comprehensive evaluation of segmentation performance. Future work will include Hausdorff Distance along with Dice and IoU to better assess the accuracy of the predicted boundaries, especially in cases where precise localization is critical. Analyzing the convergence behavior and assessing the risks of overfitting are important aspects, especially given that the model was trained for 50 epochs. Future work will include a detailed analysis of the training process, such as monitoring the loss and accuracy curves to evaluate convergence rates.

```

10/10 7s 724ms/step - binary_accuracy: 0.9936 - dice_coef: 0.3704 - iou: 0.2715 - loss: -0.3704
Epoch 32/50
10/10 0s 528ms/step - binary_accuracy: 0.9883 - dice_coef: 0.4592 - iou: 0.3243 - loss: -0.4592
Epoch 32: val_loss did not improve from -0.39043
10/10 10s 1s/step - binary_accuracy: 0.9882 - dice_coef: 0.4544 - iou: 0.3208 - loss: -0.4544 -
Epoch 33/50
10/10 0s 532ms/step - binary_accuracy: 0.9903 - dice_coef: 0.5435 - iou: 0.3834 - loss: -0.5435
Epoch 33: val_loss did not improve from -0.39043
10/10 10s 1s/step - binary_accuracy: 0.9903 - dice_coef: 0.5380 - iou: 0.3791 - loss: -0.5380 -
Epoch 34/50
10/10 0s 536ms/step - binary_accuracy: 0.9947 - dice_coef: 0.6155 - iou: 0.4676 - loss: -0.6155
Epoch 34: val_loss did not improve from -0.39043
10/10 10s 1s/step - binary_accuracy: 0.9948 - dice_coef: 0.6153 - iou: 0.4682 - loss: -0.6153 -
Epoch 35/50
10/10 0s 536ms/step - binary_accuracy: 0.9922 - dice_coef: 0.4910 - iou: 0.3484 - loss: -0.4910
Epoch 35: val_loss did not improve from -0.39043
10/10 7s 743ms/step - binary_accuracy: 0.9921 - dice_coef: 0.4878 - iou: 0.3461 - loss: -0.4878
Epoch 36/50
10/10 0s 535ms/step - binary_accuracy: 0.9896 - dice_coef: 0.3710 - iou: 0.2649 - loss: -0.3710
Epoch 36: val_loss did not improve from -0.39043
10/10 10s 1s/step - binary_accuracy: 0.9896 - dice_coef: 0.3783 - iou: 0.2695 - loss: -0.3783 -
Epoch 37/50
10/10 0s 530ms/step - binary_accuracy: 0.9912 - dice_coef: 0.4590 - iou: 0.3119 - loss: -0.4590
Epoch 37: val_loss did not improve from -0.39043
10/10 7s 731ms/step - binary_accuracy: 0.9913 - dice_coef: 0.4596 - iou: 0.3132 - loss: -0.4596
Epoch 37: early stopping

```

**Fig. 6.** Result summary with respect to epoch.

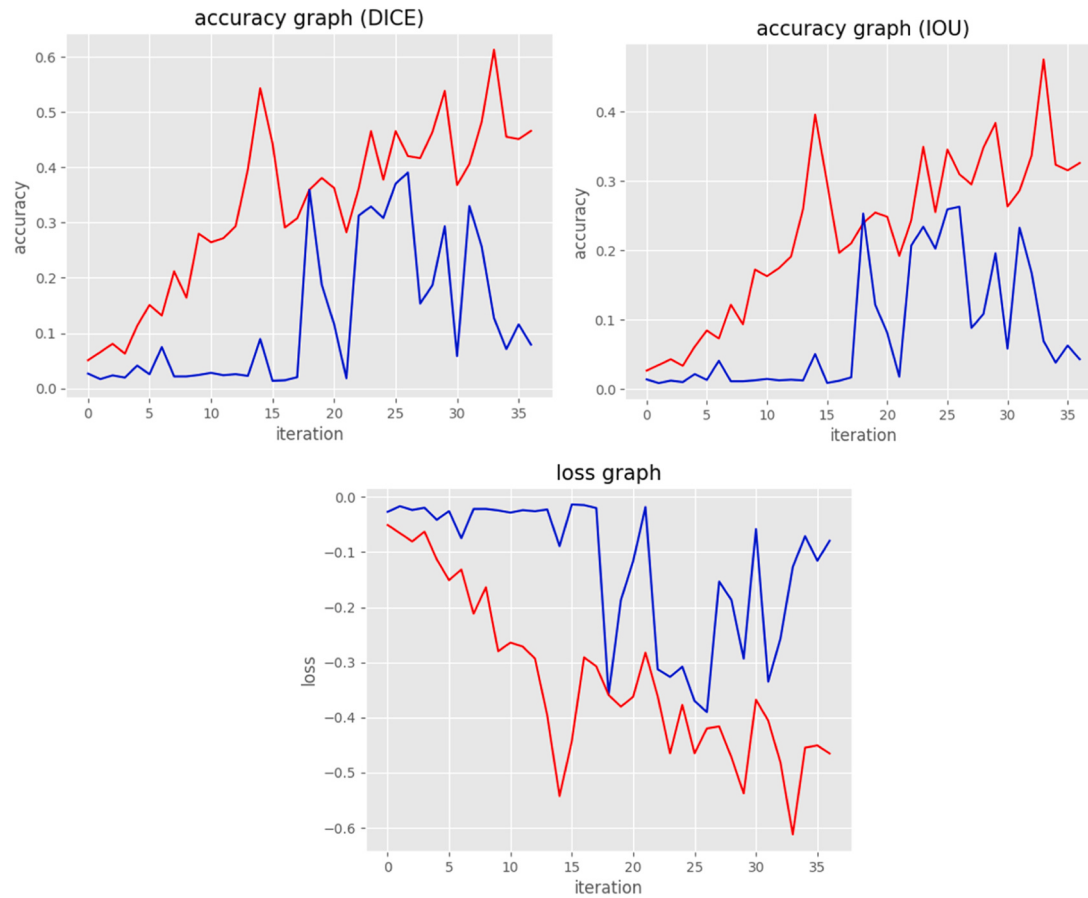


**Fig. 7.** Performance of DICE accuracy, IOU accuracy and loss graph with respect to epoch.

Additionally, techniques like early stopping, regularization, and cross-validation will be explored to mitigate overfitting and ensure that the model generalizes well to unseen data.

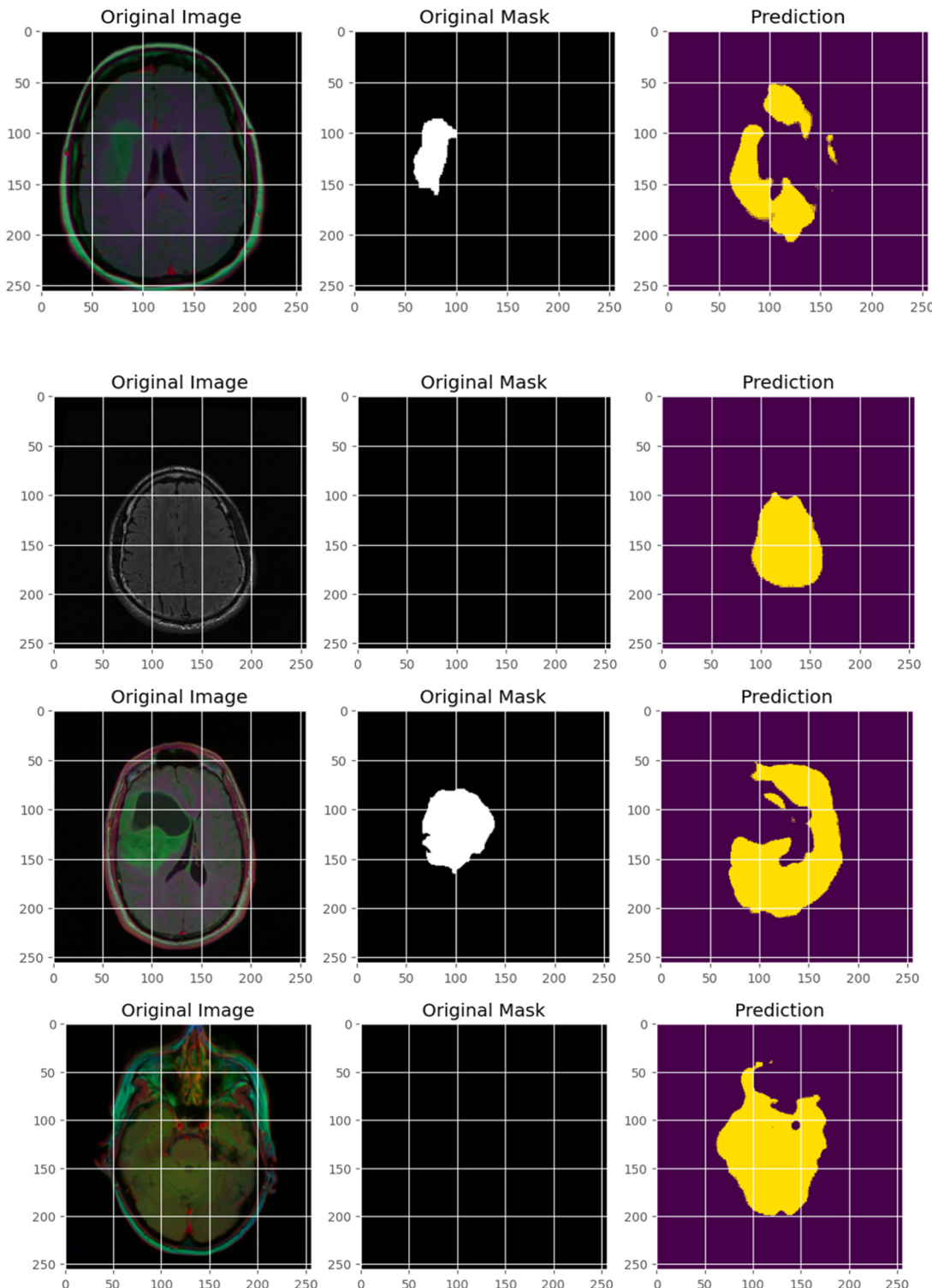
The most important factor in training and validating a model is its training parameters. Therefore, all training parameters must be set the same way for the same dataset. Having trained the network, you can use

it to segment images. It takes only a few seconds to segment images using the trained and validated model. Alternatively, clinicians may spend hours manually segmenting tumors. Doctors may be able to diagnose brain tumors more quickly and accurately by using the image segmentation procedures suggested, possibly saving the lives of many people. In Fig. 8, the validation shows 91.08 per cent accuracy, 0.0608

```

Found 393 validated image filenames.
Found 393 validated image filenames.
10/10      2s 179ms/step - binary_accuracy: 0.9108 - dice_coef: 0.1113 - iou: 0.0608 - loss: -0.1113
Test lost: -0.10432098060846329
Test IOU: 0.9047350883483887
Test Dice Coefficent: 0.05724881961941719

```

**Fig. 8.** Validation result summary with respect to epoch.**Fig. 9.** Three-panel visualization of brain MRI segmentation results.

per cent IOU, and –0.1113 percent loss.

As originally proposed, UNet was implemented in accordance with its original architecture. Consequently, we made minor changes to the network for segmentation. To make these small changes, we selected the right activation function for the final layer of the network. Another modification was made to the loss function, as well as changing the original loss function for multiclass segmentation problems. Using UNet, we were able to generate adequate visual predictions. In order to create a binary output, the predicted mask is thresholded at 0.5. In Fig. 9, this visualization shows how accurately the model segments brain regions from MRI scans.

Comparing the original mask with the predicted mask is necessary to validate the machine learning model in medical diagnostics. Models closely match original masks, allowing high-precision identification and localization of pathological features within MRI scans. MRI scans show detailed information about the patient's brain, including any possible pathologies as well as its anatomy. A medical expert has annotated this document. In a number of annotations, potential abnormalities are highlighted, such as tumors and lesions, which may indicate clinical relevance. Based on machine learning, this image shows the regions that a model was trained to identify and demarcate. The model's accuracy can also be evaluated by comparing these predictions to the expert's annotations in red.

Binary accuracy alone is not sufficient to comprehensively evaluate segmentation performance. Future work will incorporate additional segmentation-specific metrics such as precision, recall, Dice coefficient, and Intersection over Union (IoU). These metrics will provide a more detailed assessment of the model's effectiveness, particularly in capturing tumor boundaries and handling class imbalance.

## 5. Conclusion

This study presented an enhanced U-Net architecture for optimizing deep learning-based tumor segmentation. Segmentation accuracy and computational efficiency are both improved with our model thanks to the incorporation of nested skip pathways and advanced activation functions. As a result of training and validating the model on the LGG Segmentation Dataset, we achieved superior Dice coefficients and IoU scores to several existing methods. An accurate definition of tumor boundaries can be achieved using the proposed method, making diagnosis and treatment planning easier. To improve segmentation performance, we plan to incorporate multimodal MRI data into advanced deep-learning techniques, such as attention mechanisms. As a result, brain tumors can be identified and analyzed more efficiently, ultimately improving patients' quality of life. Evaluating the model's ability to generalize to unseen MRI datasets outside the LGG Segmentation Dataset is an important consideration. Future work will test the model on other publicly available MRI datasets, such as the BraTS dataset or datasets from different institutions, to assess its performance and generalization ability across varied MRI scanning protocols, patient demographics, and tumor types.

## CRediT authorship contribution statement

**Alshuhail Asma:** Writing – review & editing, Writing – original draft, Resources, Methodology, Conceptualization. **Mahmood Khalid:** Writing – original draft, Methodology, Formal analysis, Data curation. **Obayya Marwa:** Writing – original draft, Supervision, Methodology, Investigation, Conceptualization. **Aljehane Nojood O:** Writing – review & editing, Writing – original draft, Validation. **Almansour Hamad:** Writing – original draft, Validation, Methodology. **Alanazi Meshari:** Writing – review & editing, Writing – original draft, Validation, Project administration, Methodology. **Alqahtani Mohammed:** Writing – review & editing, Visualization, Validation, Software, Data curation. **Al-Hagery Mohammed Abdullah:** Writing – review & editing, Writing – original draft, Validation.

## Declaration of Competing Interest

The authors certify that they have NO affiliations with or involvement in any organization or entity with any financial interest (such as honoraria; educational grants; participation in speakers' bureaus; membership, employment, consultancies, stock ownership, or other equity interest; and expert testimony or patent-licensing arrangements), or non-financial interest (such as personal or professional relationships, affiliations, knowledge or beliefs) in the subject matter or materials discussed in this manuscript.

## Acknowledgements

This work was supported by the Deanship of Scientific Research, Vice Presidency for Graduate Studies and Scientific Research, King Faisal University, Saudi Arabia, under project Grant KFU251565. The authors extend their appreciation to the Deanship of Research and Graduate Studies at King Khalid University for funding this work through Large Research Project under grant number RGP2/26/45. Princess Nourah bint Abdulrahman University Researchers Supporting Project number (PNURSP2025R203), Princess Nourah bint Abdulrahman University, Riyadh, Saudi Arabia. The authors extend their appreciation to the Deanship of Scientific Research at Northern Border University, Arar, KSA for funding this research work through the project number ‘NBU-FPEJ-2025-1180-03. The authors are thankful to the Deanship of Graduate Studies and Scientific Research at University of Bisha for supporting this work through the Fast-Track Research Support Program.

## References

- [1] A. Patel, Benign vs malignant tumors, *JAMA Oncol.* 6 (9) (Sep. 2020) 1488, <https://doi.org/10.1001/jamaonc.2020.2592>.
- [2] P. Rani, S.P. Yadav, P.N. Singh, M. Almusawi, Real-world case studies: transforming mental healthcare with natural language processing, in: A. Mishra, S.P. Yadav, M. Kumar, S.M. Biju, G.C. Deka (Eds.), *Demystifying the Role of Natural Language Processing (NLP) in Mental Health*, IGI Global, 2025, pp. 303–324, <https://doi.org/10.4018/979-8-3693-4203-9.ch016>.
- [3] A. İşın, C. Direkoglu, M. Şah, Review of MRI-based brain tumor image segmentation using deep learning methods, *Procedia Comput. Sci.* 102 (2016) 317–324, <https://doi.org/10.1016/j.procs.2016.09.407>.
- [4] A. Md.Sattar, M. Kr. Ranjan, Automatic cancer detection using probabilistic convergence theory, in: K. Raza (Ed.), *Computational Intelligence in Oncology* (in *Studies in Computational Intelligence*), Springer Singapore, Singapore, 2022, pp. 111–122, [https://doi.org/10.1007/978-981-16-9221-5\\_6](https://doi.org/10.1007/978-981-16-9221-5_6), vol. 1016.
- [5] M.S. Pathan, A. Nag, M.M. Pathan, S. Dev, Analyzing the impact of feature selection on the accuracy of heart disease prediction, *Healthc. Anal.* 2 (Nov. 2022) 100060, <https://doi.org/10.1016/j.health.2022.100060>.
- [6] G. Sivapalan, K.K. Nundy, S. Dev, B. Cardiff, D. John, ANNet: a lightweight neural network for ECG anomaly detection in IoT edge sensors, *IEEE Trans. Biomed. Circuits Syst.* 16 (1) (Feb. 2022) 24–35, <https://doi.org/10.1109/TBCAS.2021.3137646>.
- [7] P. Rani, U.C. Garjola, H. Abbas, A predictive IoT and cloud framework for smart healthcare monitoring using integrated deep learning model, *NJF Intell. Eng.* 1 (1) (2024) 53–65.
- [8] P. Rani, D.S. Mohan, S.P. Yadav, G.K. Rajput, M.A. Farouni, Sentiment analysis and emotional recognition: enhancing therapeutic interventions, in: A. Mishra, S.P. Yadav, M. Kumar, S.M. Biju, G.C. Deka (Eds.), *Demystifying the Role of Natural Language Processing (NLP) in Mental Health*, IGI Global, 2025, pp. 283–302, <https://doi.org/10.4018/979-8-3693-4203-9.ch015>.
- [9] J. Hu, X. Gu, X. Gu, Mutual ensemble learning for brain tumor segmentation, *Neurocomputing* 504 (Sep. 2022) 68–81, <https://doi.org/10.1016/j.neucom.2022.06.058>.
- [10] X. Liu, L. Song, S. Liu, Y. Zhang, A review of deep-learning-based medical image segmentation methods, *Sustainability* 13 (3) (Jan. 2021) 1224, <https://doi.org/10.3390/su13031224>.
- [11] O. Ronneberger, P. Fischer, T. Brox, U-Net: convolutional networks for biomedical image segmentation, in: N. Navab, J. Hornegger, W.M. Wells, A.F. Frangi (Eds.), *Medical Image Computing and Computer-Assisted Intervention – MICCAI 2015*, vol. 9351, Springer International Publishing, Cham, 2015, pp. 234–241, [https://doi.org/10.1007/978-3-319-24574-4\\_28](https://doi.org/10.1007/978-3-319-24574-4_28) (in *Lecture Notes in Computer Science*).
- [12] S. Verma, et al., An automated face mask detection system using transfer learning based neural network to preventing viral infection, *Expert Syst.* (2024) e13507.
- [13] S. Dev, A. Nautiyal, Y.H. Lee, S. Winkler, CloudSegNet: a deep network for nychthemeron cloud image segmentation, *IEEE Geosci. Remote Sens. Lett.* 16 (12) (Dec. 2019) 1814–1818, <https://doi.org/10.1109/LGRS.2019.2912140>.

- [14] S. Dev, Y.H. Lee, S. Winkler, Color-based segmentation of sky/cloud images from ground-based cameras, *IEEE J. Sel. Top. Appl. Earth Obs. Remote Sens.* 10 (1) (Jan. 2017) 231–242, <https://doi.org/10.1109/JSTARS.2016.2558474>.
- [15] M. Jain, C. Meegan, S. Dev, Using gans to augment data for cloud image segmentation task. 2021 IEEE International Geoscience and Remote Sensing Symposium IGARSS, IEEE, Brussels, Belgium, Jul. 2021, pp. 3452–3455, <https://doi.org/10.1109/IGARSS47720.2021.9554993>.
- [16] N. Bien, et al., Deep-learning-assisted diagnosis for knee magnetic resonance imaging: development and retrospective validation of MRNet, *PLoS Med.* 15 (11) (Nov. 2018) e1002699, <https://doi.org/10.1371/journal.pmed.1002699>.
- [17] Z. Zhou, M.M. Rahman Siddiquee, N. Tajbakhsh, J. Liang, UNet++: a nested U-net architecture for medical image segmentation (in Lecture Notes in Computer Science), in: D. Stoyanov, Z. Taylor, G. Carneiro, T. Syeda-Mahmood, A. Martel, L. Maier-Hein, J.M.R.S. Tavares, A. Bradley, J.P. Papa, V. Belagiannis, J. C. Nascimento, Z. Lu, S. Conjeti, M. Moradi, H. Greenspan, A. Madabhushi (Eds.), *Deep Learning in Medical Image Analysis and Multimodal Learning for Clinical Decision Support*, Springer International Publishing, Cham, 2018, pp. 3–11, [https://doi.org/10.1007/978-3-030-00889-5\\_1](https://doi.org/10.1007/978-3-030-00889-5_1). vol. 11045.
- [18] G.P. Mazzara, R.P. Velthuizen, J.L. Pearlman, H.M. Greenberg, H. Wagner, Brain tumor target volume determination for radiation treatment planning through automated MRI segmentation, *Int. J. Radiat. Oncol. Biol. Phys.* 59 (1) (May 2004) 300–312, <https://doi.org/10.1016/j.ijrobp.2004.01.026>.
- [19] S. Bauer, R. Wiest, L.-P. Nolte, M. Reyes, A survey of MRI-based medical image analysis for brain tumor studies, *Phys. Med. Biol.* 58 (13) (Jul. 2013) R97–R129, <https://doi.org/10.1088/0031-9155/58/13/R97>.
- [20] T.L. Jones, T.J. Byrnes, G. Yang, F.A. Howe, B.A. Bell, T.R. Barrick, Brain tumor classification using the diffusion tensor image segmentation (D-SEG) technique, *Neuro-Oncol.* (Aug. 2014) nou159, <https://doi.org/10.1093/neuonc/nou159>.
- [21] P. Rani, S. Verma, S.P. Yadav, B.K. Rai, M.S. Naruka, D. Kumar, Simulation of the lightweight blockchain technique based on privacy and security for healthcare data for the cloud system, *Int. J. E-Health Med. Commun.* 13 (4) (2022) 1–15.
- [22] S. Bakas, et al., Advancing the cancer genome atlas glioma MRI collections with expert segmentation labels and radiomic features, *Sci. data* 4 (1) (2017) 1–13.
- [23] K. Aldape, et al., Challenges to curing primary brain tumours, *Nat. Rev. Clin. Oncol.* 16 (8) (2019) 509–520.
- [24] M. Togaçar, Z. Cömert, B. Ergen, Classification of brain MRI using hyper column technique with convolutional neural network and feature selection method, *Expert Syst. Appl.* 149 (Jul. 2020) 113274, <https://doi.org/10.1016/j.eswa.2020.113274>.
- [25] S. Ahuja, B.K. Panigrahi, T. Gandhi, Transfer learning based brain tumor detection and segmentation using superpixel technique. 2020 International Conference on Contemporary Computing and Applications (IC3A), IEEE, Lucknow, India, Feb. 2020, pp. 244–249, <https://doi.org/10.1109/IC3A48958.2020.923306>.
- [26] T.M. Hsieh, Y.-M. Liu, C.-C. Liao, F. Xiao, I.-J. Chiang, J.-M. Wong, Automatic segmentation of meningioma from non-contrasted brain MRI integrating fuzzy clustering and region growing, *BMC Med. Inf. Decis. Mak.* 11 (1) (Dec. 2011) 54, <https://doi.org/10.1186/1472-6947-11-54>.
- [27] L. Szilagyi, L. Lefkovits, B. Benyo, Automatic brain tumor segmentation in multispectral MRI volumes using a fuzzy c-means cascade algorithm. 2015 12th International Conference on Fuzzy Systems and Knowledge Discovery (FSKD), IEEE, Zhangjiajie, China, Aug. 2015, pp. 285–291, <https://doi.org/10.1109/FSKD.2015.7381955>.
- [28] J. Juan-Albaracín, et al., Automated glioblastoma segmentation based on a multiparametric structured unsupervised classification, *PLoS One* 10 (5) (May 2015) e0125143, <https://doi.org/10.1371/journal.pone.0125143>.
- [29] C.L. Choudhury, C. Mahanty, R. Kumar, B.K. Mishra, Brain tumor detection and classification using convolutional neural network and deep neural network. 2020 International Conference on Computer Science, Engineering and Applications (ICCSEA), IEEE, Gunupur, India, Mar. 2020, pp. 1–4, <https://doi.org/10.1109/ICCSEA49143.2020.9132874>.
- [30] S.Kr Ghosh, B. Biswas, A. Ghosh, Restoration of mammograms by using deep convolutional denoising auto-encoders (in Advances in Intelligent Systems and Computing), in: H.S. Behera, J. Nayak, B. Naik, D. Pelusi (Eds.), *Computational Intelligence in Data Mining*, Springer Singapore, Singapore, 2020, pp. 435–447, [https://doi.org/10.1007/978-981-13-8676-3\\_38](https://doi.org/10.1007/978-981-13-8676-3_38). vol. 990.
- [31] A. Rehman, M.A. Khan, T. Saba, Z. Mahmood, U. Tariq, N. Ayesha, Microscopic brain tumor detection and classification using 3D CNN and feature selection architecture, *Microsc. Res. Tech.* 84 (1) (Jan. 2021) 133–149, <https://doi.org/10.1002/jemt.23597>.
- [32] P. Tripathi, V. Kumar Singh, M. Chandra Trivedi, Brain tumor segmentation in magnetic resonance imaging using OKM approach, *Mater. Today Proc.* 37 (2021) 1334–1340, <https://doi.org/10.1016/j.matpr.2020.06.548>.
- [33] A.H. Thias, A.F. Al Mubarok, A. Handayani, D. Danudirdjo, T.E. Rajab, Brain tumor semi-automatic segmentation on MRI T1-weighted images using active contour models. 2019 International Conference on Mechatronics, Robotics and Systems Engineering (MoRSE), IEEE, Bali, Indonesia, Dec. 2019, pp. 217–221, <https://doi.org/10.1109/MoRSE48060.2019.8998651>.
- [34] A. Çinar, M. Yıldırım, Detection of tumors on brain MRI images using the hybrid convolutional neural network architecture, *Med. Hypotheses* 139 (Jun. 2020) 109684, <https://doi.org/10.1016/j.mehy.2020.109684>.
- [35] S.A. Abdelaziz Ismail, A. Mohammed, H. Hefny, An enhanced deep learning approach for brain cancer MRI images classification using residual networks, *Artif. Intell. Med.* 102 (Jan. 2020) 101779, <https://doi.org/10.1016/j.artmed.2019.101779>.
- [36] M. Havaei, et al., Brain tumor segmentation with Deep Neural Networks, *Med. Image Anal.* 35 (Jan. 2017) 18–31, <https://doi.org/10.1016/j.media.2016.05.004>.
- [37] K. Kamnitsas, et al., Efficient multi-scale 3D CNN with fully connected CRF for accurate brain lesion segmentation, *Med. Image Anal.* 36 (Feb. 2017) 61–78, <https://doi.org/10.1016/j.media.2016.10.004>.
- [38] U. Baid, et al., A novel approach for fully automatic intra-tumor segmentation with 3D U-Net architecture for gliomas, *Front. Comput. Neurosci.* 14 (Feb. 2020) 10, <https://doi.org/10.3389/fncom.2020.00010>.
- [39] W.M. Jwaid, Z.S.M. Al-Husseini, A.H. Sabry, Development of brain tumor segmentation of magnetic resonance imaging (MRI) using U-Net deep learning, *EEJET* 4 (9(12)) (Aug. 2021) 23–31, <https://doi.org/10.15587/1729-4061.2021.238957>.
- [40] A. Atiyah, K. Ali, Brain MRI images segmentation based on U-net architecture, *IJEEE* 18 (1) (Jun. 2022) 21–27, <https://doi.org/10.37917/ijeee.18.1.3>.
- [41] C. Yan, J. Ding, H. Zhang, K. Tong, B. Hua, S. Shi, SEResU-net for multimodal brain tumor segmentation, *IEEE Access* 10 (2022) 117033–117044, <https://doi.org/10.1109/ACCESS.2022.3214309>.
- [42] A.A. Pravitasari, et al., UNet-VGG16 with transfer learning for MRI-based brain tumor segmentation, *Telkomnika* 18 (3) (Jun. 2020) 1310, <https://doi.org/10.12928/telkomnika.v18i3.14753>.
- [43] I. Aboussaleh, J. Riffi, K.E. Fazazy, M.A. Mahraz, H. Tairi, Efficient U-net architecture with multiple encoders and attention mechanism decoders for brain tumor segmentation, *Diagnostics* 13 (5) (Feb. 2023) 872, <https://doi.org/10.3390/diagnostics13050872>.
- [44] Q. Zhang, W. Qi, H. Zheng, X. Shen, CU-Net: a U-net architecture for efficient brain-tumor segmentation on Brats 2019 dataset. 2024 4th International Conference on Machine Learning and Intelligent Systems Engineering (MLISE), IEEE, Zhuhai, China, Jun. 2024, pp. 255–258, <https://doi.org/10.1109/MLISE62164.2024.10674119>.
- [45] A.A. Asiri, et al., Brain tumor detection and classification using fine-tuned CNN with ResNet50 and U-net model: a study on TCGA-LGG and TCIA dataset for MRI applications, *Life* 13 (7) (Jun. 2023) 1449, <https://doi.org/10.3390/life13071449>.
- [46] M.U. Rehman, S. Cho, J.H. Kim, K.T. Chong, BU-Net: brain tumor segmentation using modified U-net architecture, *Electronics* 9 (12) (Dec. 2020) 2203, <https://doi.org/10.3390/electronics9122203>.
- [47] J. Long, E. Shelhamer, T. Darrell, Fully convolutional networks for semantic segmentation, *Proc. IEEE Conf. Comput. Vis. Pattern Recognit.* (2015) 3431–3440. Accessed: Mar. 05, 2025. [Online]. Available: [http://openaccess.thecvf.com/content\\_cvpr\\_2015/html/Long\\_Fully\\_Convolutional\\_Networks\\_2015\\_CVPR\\_paper.html](http://openaccess.thecvf.com/content_cvpr_2015/html/Long_Fully_Convolutional_Networks_2015_CVPR_paper.html).
- [48] G. Michalopoulos, H.C. Pitot, Primary culture of parenchymal liver cells on collagen membranes. Morphological and biochemical observations, *Exp. Cell Res.* 94 (1) (Aug. 1975) 70–78, [https://doi.org/10.1016/0014-4827\(75\)90532-7](https://doi.org/10.1016/0014-4827(75)90532-7).
- [49] C. Nwankpa, W. Ijomah, A. Gachagan, S. Marshall, Activation functions: comparison of trends in practice and research for deep learning, *arXiv* (2018), <https://doi.org/10.48550/ARXIV.1811.03378>.